

Deformation and Ductile Fracture by Using Mesoscale Finite Element Simulations

Shigeru YONEMURA* Masahiro KUBO
Yusuke TSUNEMI Daisuke MAEDA
Akihiro UENISHI Satoshi HIROSE
Yoshihiro SUWA Takashi YASUTOMI

Abstract

The deformation of polycrystalline steels is extremely heterogeneous both intergranularly and intragranularly. In steel development, heterogeneity at various scales has been controlled in order to realize superior characteristics at the macro scale. In the present study, [1] in-situ observation of microstructure evolution was conducted for uniaxial and biaxial tensile deformation using the microscopic biaxial tensile system with electron back scatter diffraction (EBSD) with scanning electron microscope (SEM) analysis. Biaxial tension deformation was simulated by using crystal plasticity FE simulation, and the differential work hardening behavior under biaxial tension in polycrystalline IF (interstitial free) steel was microscopically explained from the viewpoints of microstructural evolution. [2] Voids nucleation of dual phase steel with 10% martensite volume fraction was analyzed by meso-scale FE simulations. FE simulations have satisfactorily predicted the strain localization in ferrite, the fracture of martensite islands, and the martensite islands subjected to interface decohesions. Furthermore, the effects of the strength between two phases on the ductile fracture of DP steel is investigated using finite element simulations with the continuum damage mechanics (CDM) model.

1. Introduction

Polycrystalline steels are heterogeneous at various microscopic scales such as grains, second-phase particles, and dislocation cell walls. Macroscopic mechanical properties appear as a composite material effect of these. For example, texture affects mechanical properties such as elasticity, plasticity, and fracture characteristics significantly, and therefore texture control is an important factor for controlling the microstructure. In particular, deep drawability, which is estimated from an r -value, plays a significant role in the formability. The high r -values are ascribed to the texture with a strong γ -fiber ($\langle 111 \rangle$ component parallel to ND). Ti-added interstitial free (IF) steel for which interstitial type solute elements are reduced as much as possible has been developed and practically used.

Meanwhile, an example of the active use of heterogeneous structure in steel materials is improvement in the strength-tensile elonga-

tion balance of dual phase (DP) steel. DP steel, composed of hard martensite islands embedded into a softer ferrite matrix, has been increasingly used for automobiles because they offer an excellent compromise between high strength and tensile elongation. Usually, the metallographic structure of practical steel sheets often becomes a composite structure. The volume fraction of the hard phase and optimization of its size, shape, and dispersion state are important structure control factors.¹⁾

In recent years, numerical simulations have been increasingly used to evaluate the macroscopic mechanical properties from material microstructure against the background of the rapid progress of computer power. Numerical analysis using the finite element method (FEM) in which heterogeneity can be taken into account can evaluate the elementary processes of deformation, clarification of its mechanism, the material's microscopic structure changes, and mac-

* Senior Researcher, Dr. Eng., Application Technology Research Lab., Steel Research Laboratories
20-1 Shintomi, Futtsu City, Chiba Pref. 293-8511

rososcopic deformation characteristics in a quantitative way.

In this study, a biaxial tensile test system in a scanning electron microscope (SEM) vacuum chamber that allowed *in-situ* observation was used to clarify the characteristics of microscopic structure changes of IF steel under biaxial tensile deformation; and the mechanism of differential work hardening behavior where work hardening in equal biaxial deformation was larger than that in uniaxial tensile deformation was studied by crystal plasticity FEM analysis. Subsequently, ductile fracture on DP steel was analyzed using the mesoscale FEM to which actual structure was reflected; the authors show that the fracture of martensite and the fracture at the interface between martensite and ferrite can be simulated. Moreover, the effects of strength differences between the two phases of DP steel on macroscopic deformation characteristics were studied by finite element simulations (analysis) using the continuum damage mechanics (CDM) model.

2. Effects of Microscopic Structure of IF Steel on Differential Work Hardening Behavior

Plastic anisotropy and work hardening behavior are the most important material properties in sheet metal forming. Usually, material properties are evaluated in uniaxial tensile tests, but materials are subjected to multi-axial loads in sheet forming processes. The biaxial tensile test using cruciform specimens has been developed²⁾ to evaluate the work hardening behavior of anisotropic sheet metals under biaxial tension. The contours of plastic work in stress spaces for various materials have been evaluated and much knowledge has been reported to date.^{3,4)} **Figure 1** shows the results of the measurement of contours of plastic work for IF steel sheets (with a thickness of 1.2 mm and an average *r* value of 1.87) using the biaxial tensile test system.⁵⁾

These contours of plastic work have been normalized by σ_0 corresponding to a specific ϵ_0^p . The IF steel exhibits definite differential hardening; the work contour for $\epsilon_0^p=0.0005$ is very close to the von Mises yield locus, and is elongated in the equibiaxial tension direction as the material work hardens. The yield locus develops rapidly around equibiaxial tension, which means that the work hardening behavior has anisotropy under biaxial tension.⁴⁾ In addition, Kubo et

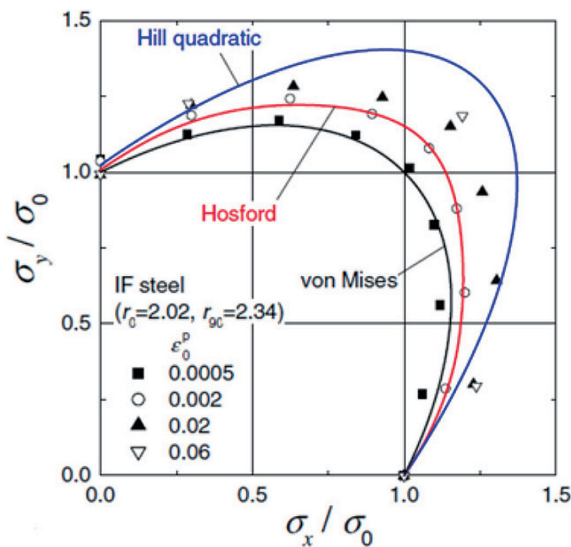


Fig. 1 Experimental data comprising contours of plastic work for IF steel⁵⁾

al.⁶⁾ measured the curve of the equibiaxial tensile stress-equivalent plastic strain in a hydrostatic bulge test and studied the relationship between the ratio to uniaxial tensile stress and equivalent plastic strain (**Fig. 2**), but differential hardening behavior has not been microscopically explained from the viewpoints of microstructural evolution.

Regarding the microstructural factors of differential hardening on IF steel, Ikematsu et al.⁷⁾ focused on the different types of dislocation substructure that were formed under uniaxial tension and equibiaxial tension, revealing that differential hardening behavior may be caused by the difference of the selection of activated slip systems between biaxial and uniaxial tensions. Other factors are the microstructural evolution and effects of internal stress caused by the heterogeneous deformation behavior of microstructural components such as grains, particles, and dislocation cell walls, but they have not been studied. Therefore, this study clarifies the characteristics of structure changes on IF steel in uniaxial tensile and biaxial tensile deformation by *in-situ* observation, creates a finite element model for material structure from such observation data, and studies the differential hardening mechanism by crystal plasticity FEM analysis.

2.1 Experimental procedures

The sample used was ultra-low carbon IF steel (270 MPa-class steel sheet 1.6 mm thick with an average *r* value of 1.7) that would show differential work hardening behavior (**Fig. 2**). The biaxial tensile test system⁸⁾ in an SEM vacuum chamber shown in **Fig. 3** was used to observe structure changes in uniaxial and equal biaxial tensile deformation. The test system was tilted by approximately 60° in the vacuum chamber and a tensile test (initial strain rate: 1.0×10^{-3} /s) was carried out while the structure was observed and analyzed using the SEM and electron back scatter diffraction (EBSD). In the case of a uniaxial tensile test, only the y-axis direction in **Fig. 2** is utilized. In case the of a biaxial tensile test, the displacement of each crosshead was controlled to synchronize them. The material microstructure in a field of view with 200 μm sides was observed *in-situ* during the tensile test while the tension was maintained. The strain during this test was measured from the distance between two triple crystal points with reference to their locations.

2.2 Numerical analysis procedures

2.2.1 Crystal plasticity model

As the crystal plasticity model, the model proposed by Hoc et al.⁹⁾ that had been applied to IF steel was used. In this model, the

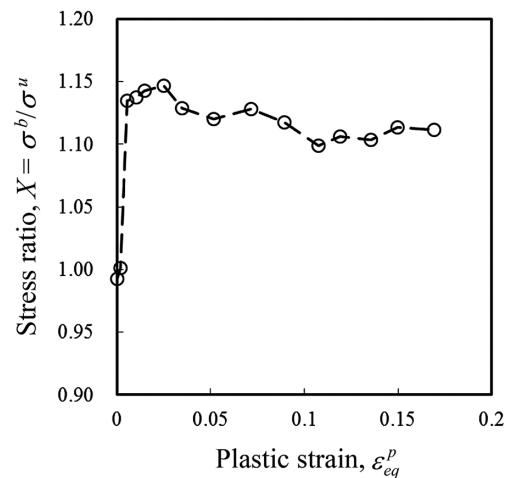


Fig. 2 Differential hardening behavior of IF steel sheet⁶⁾

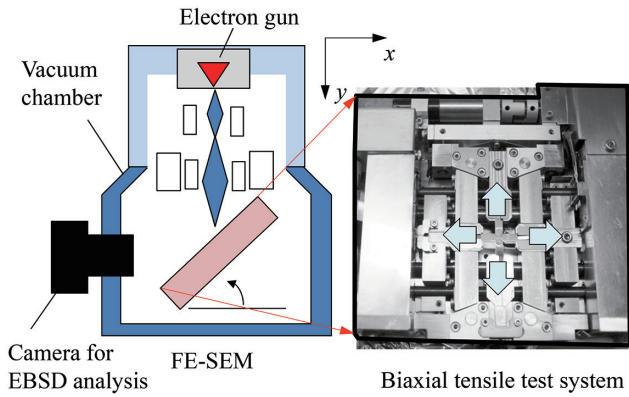


Fig. 3 Experimental apparatus for uniaxial and biaxial test with SEM-EBSD analysis⁸⁾

slip rate of each slip system is calculated with the following formula.

$$\dot{\gamma}^{\alpha} = \begin{cases} 0 & \text{if } |\tau^{\alpha}| \leq \tau_c^{\alpha} \\ \dot{\gamma}_0 \left(\frac{|\tau^{\alpha}| - \tau_c^{\alpha}}{\tau_0} \right)^n \text{sign}(\tau^{\alpha}) & \text{if } |\tau^{\alpha}| > \tau_c^{\alpha} \end{cases} \quad (1)$$

Where, $\dot{\gamma}_0$ is the reference strain rate, τ^{α} is the resolved shear stress working on the slip system, τ_c^{α} is the critical resolved shear stress, τ_0 is the frictional resistance that depends on the temperature, n is the reciprocal of the strain rate sensitivity exponent, and $\dot{\gamma}_0$, τ_0 , and n are material constants. The work hardening phenomenon is given by the following formula as development of the critical resolved shear stress (τ_c^{α}).

$$\tau_c^{\alpha} = \tau_0 + \tau_{\mu}^{\alpha} = \tau_0 + \mu b \sqrt{\sum_{\beta} d^{\alpha\beta} \rho^{\beta}} \quad (2)$$

Where, μ is the shear modulus, b is the magnitude of the Burgers vector, $d^{\alpha\beta}$ is the interaction matrix indicating the effect of the dislocation density of slip system β on the critical resolved shear stress of slip system α , ρ^{α} is the dislocation density of slip system α , and μ , b , and $d^{\alpha\beta}$ are the material constants. The dislocation density (ρ^{α}) is expressed with the following formula as its time evolution.

$$\begin{aligned} \dot{\rho}^{\alpha} &= \frac{1}{b} \left(\frac{1}{L^{\alpha}} - 2Y_c \rho^{\alpha} \right) |\dot{\gamma}^{\alpha}| \quad (\text{no sum on } \alpha), \quad \rho^{\alpha}(0) = \rho_0 \\ L^{\alpha} &= K \left(\sum_{\beta \neq \alpha} \rho^{\beta} \right)^{-\frac{1}{2}} \end{aligned} \quad (3)$$

Where, L^{α} is the mean free path of the mobile dislocation in the slip system α , Y_c denotes the characteristic length associated with the annihilation process of dislocation dipoles, and K is a material constant that determines the intersection effect by forest dislocation. The formula above expresses an increase in the dislocation density by forest dislocation and saturation of the dislocation density by pair annihilation. In the analysis, 24 slip systems of $\{110\}\langle 111 \rangle$ and $\{112\}\langle 111 \rangle$ were supposed and the weights for the interaction matrix ($d^{\alpha\beta}$) (Table 1) were changed based on the relationship between the directions of the Burgers vectors in the slip systems and slip planes. Material constants that Hoc et al.⁹⁾ had used for the analysis of Ti-added IF steel were used.

2.2.2 Finite element model and boundary conditions

A finite element model was generated from image data of the microstructure obtained by the SEM-EBSD method and crystal orientation distribution (Fig. 4).¹⁰⁾ Crystal orientation distribution was measured at an interval of $1 \mu\text{m}$ in the area ($200 \times 200 \mu\text{m}$). Orientation imaging microscopy (OIM) analysis was used to create crystal grains where when the misorientation between adjacent measure-

Table 1 Interaction matrix of dislocation⁹⁾

Slip systems	$\{110\} \cap \{110\}$	$\{110\} \cap \{112\}$	$\{112\} \cap \{112\}$
Same	d_0	—	$k_{s0} d_0$
Collinear	$k_1 d_0$	$k_{r1} d_0$	$k_{s0} k_1 d_0$
Not collinear	$k_2 k_1 d_0$	$k_{r2} k_{r1} d_0$	$k_{s0} k_2 k_1 d_0$

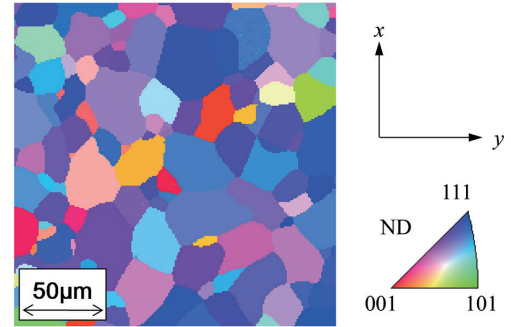


Fig. 4 Inverse pole figure obtained by the SEM-EBSD method¹⁰⁾

ment points was five degrees or more, they were determined as grain boundaries and the mean orientation representing each grain was determined. In addition, an 8-node solid element was created for each measurement point and an analysis model to which the representative orientations of the crystal grains belonging to the element had been reflected was created. In the analysis model, an element was arranged in the thickness direction and divided into 40 000 elements. Where, the x direction is the material's rolling direction and the y direction is the direction orthogonal to the rolling direction. Displacement equivalent to uniaxial and equal biaxial tension was applied to the nodal points at the end faces of the x and y directions in the analysis model.

2.3 Results and considerations

2.3.1 In-situ observation of microstructural and textural evolution by the SEM/EBSD method⁶⁾

The mechanism of the abovementioned differential hardening is examined from the viewpoint of the microstructural evolution in uniaxial and biaxial tensile states. Figures 5 and 6 show the microstructural evolution during uniaxial and biaxial tensile tests in the microscopic scale. In these figures two types of maps before deformation and two levels of strain are illustrated. The maps are the inverse pole figure (IPF) and the Taylor factor¹¹⁾ map. The IPF maps observed in the normal direction (ND) are employed to indicate the distribution of crystal orientation.^{6, 8, 12)} Taylor factors were calculated for 40 000 observation points, assuming 24 slip systems of $\{110\}\langle 111 \rangle$ and $\{112\}\langle 111 \rangle$ and the same critical resolved shear stress (CRSS) for both families of slip systems.

IF steel is ascribed to their textures with a strong γ -fiber $\langle 111 \rangle$ component parallel to ND. The surface roughness grows with the progress of tensile deformation, which makes measurement difficult. However, observation by focusing on the fact that there are crystal grains for which the crystal orientations change as a result of crystal rotation and focusing on the same crystal grains shows that orientations change in the crystal grains (figures in the upper row of Fig. 5). On the other hand, in the equibiaxial tensile deformation, development of the ND// $\langle 111 \rangle$ and $\langle 100 \rangle$ orientations due to the deformation and orientation change in the crystal grains can be seen (figures in the upper row of Fig. 6). When comparing the Taylor factors between the uniaxial and equal biaxial tensile deformation, for the

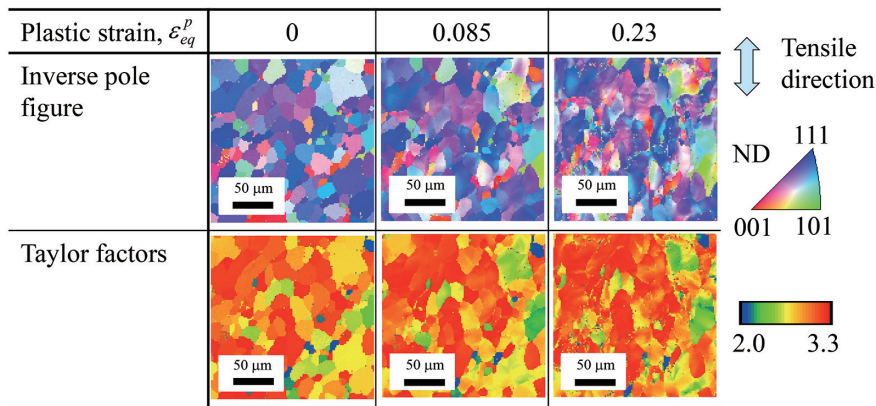


Fig. 5 IPF and Taylor factors maps during uniaxial tensile test⁶⁾

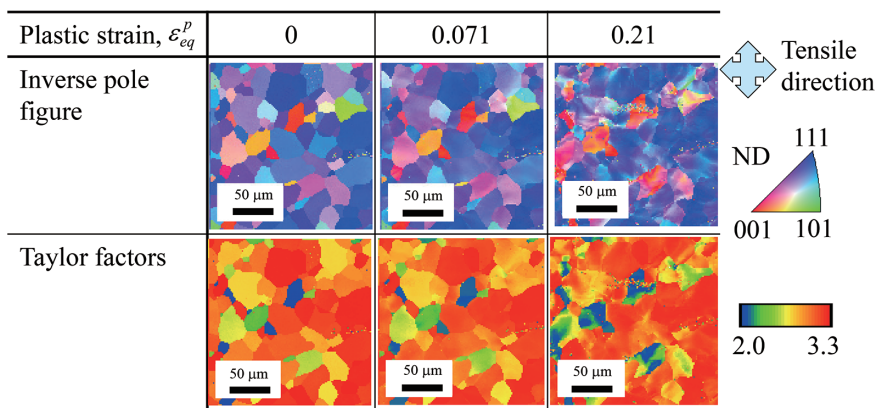


Fig. 6 IPF and Taylor factors maps during biaxial tensile test⁶⁾

equal biaxial tension, they change from dark blue to red and their change is wider than changes for the uniaxial tensile deformation. For the uniaxial tensile deformation, the Taylor factors tend to increase for almost all crystal grains as the deformation progresses, while for the equal biaxial tensile deformation, some factors of crystal grains increase and others decrease.

The mechanism of different work hardening behavior will be considered below. In the equibiaxial tensile deformation, the difference between the Taylor factor values expanded as the deformation progressed compared to the uniaxial tensile deformation. It can be assumed from this fact that for the equibiaxial tensile deformation, as the deformation progressed, the differences in deformation resistance between crystal grains became larger, which made heterogeneous deformation between the crystal grains more obvious. In addition, orientation changes were seen in the crystal grains in both uniaxial and equal biaxial tensile deformation. This is considered to be caused by heterogeneous deformation in the grains originated in the crystal grains' crystal orientations and the existence of adjacent grains surrounding them. Material structure changes due to this type of deformation are one possible factor of the different work hardening behavior.

2.3.2 Biaxial tensile simulation of IF steel by the crystal plasticity FEM

To consider the observed anisotropic hardening mechanism, uniaxial and equal biaxial tensile deformation was simulated by the crystal plasticity FEM. Figure 7 shows the relationship between the equivalent plastic strain (ϵ_{eq}^p) and the ratio ($X = \sigma^b/\sigma^u$) of the equal

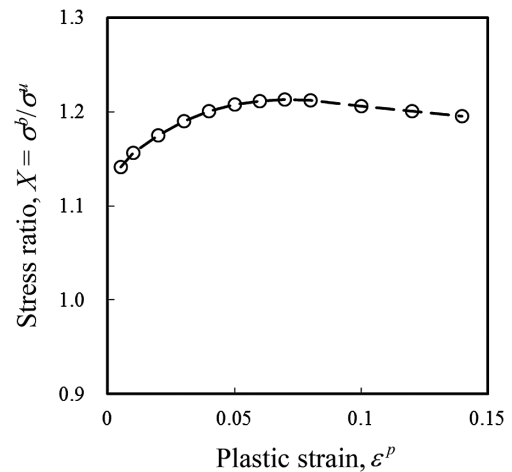


Fig. 7 Differential hardening behavior of IF steel sheet by crystal plasticity analysis¹⁰⁾

biaxial tensile stress (σ^b) to the uniaxial tensile stress (σ^u). The calculated stress ratio (X) increased until the plastic strain (ϵ_{eq}^p) reached approximately 0.07, became maximum when ϵ_{eq}^p was close to 0.07, and then gradually decreased. When comparing these results to the experimental results in Fig. 2, although the magnitude of the anisotropy and that of the plastic strain at which the maximum value was obtained are different, the results well reproduce the tendency of the experiment in which the work hardening is larger for the equal biaxial

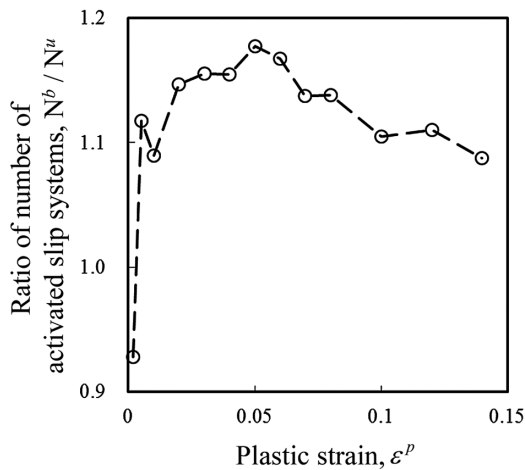


Fig. 8 Ratio of number of activated slip system of uniaxial and biaxial deformation

tensile deformation in the low strain region and after that the ratio of the uniaxial tensile stress to the equal biaxial tensile stress gradually becomes smaller.

Dislocation interaction affects the differential work hardening behavior on IF steel.¹³⁾ Therefore, we focused on the number of activated slip systems as an index to show the strength of dislocation interaction and evaluated its effect. Slip in a slip system is calculated for each integration point in each element. In our study, the average number of activated slip systems was calculated for each integration point and the ratio of the number of activated slip systems in the equal biaxial tensile deformation (N^b) to that in the uniaxial tensile deformation (N^u) was calculated (Fig. 8). The ratio between the numbers of activated slip systems calculated significantly increased at the initial stage of the deformation, became maximum when the plastic strain was close to 0.05, and after that gradually decreased. This tendency reproduces that in the anisotropic work hardening behavior in Fig. 7, so interaction between slip systems is one possible factor of anisotropic hardening.

The deforming stress of a material is the sum total of the stress that moving dislocations existing in each slip system receive and it is caused by the self-hardening of dislocations in the same slip system and latent hardening of dislocations belonging to other slip systems.¹³⁾ In the equal biaxial tensile deformation, large work hardening was seen possibly due to the interaction between slip systems at the beginning of the deformation and new slip systems that started moving by crystal rotation.

3. Simulation of Ductile Fracture on DP Steel¹⁴⁾

3.1 Experimental procedures

A DP steel sheet with a tensile strength of 590 MPa class was used for the experiment. In this experiment, steel with the chemical composition of Fe-0.067C-0.5Si-1.5Mn (mass%) was vacuum melted, finish-rolled at 800°C to a thickness of 1.8 mm, air-cooled to 650°C, and then water-quenched to room temperature to create DP steel consisting of ferrite and martensite.¹⁵⁾ The martensite volume fraction of this steel sheet is 10%.

A tensile micro-machine installed on a laser microscope was used for the *in-situ* observation of void formation behavior on the steel sheet due to tensile deformation. A tensile test specimen 0.08 mm thick was cut out from the center of the thickness from the 1.8-mm thick steel sheet and a notch with a radius of 0.4 mm was pro-

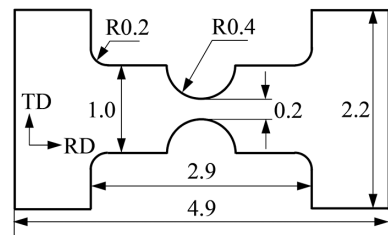


Fig. 9 Micro-tensile specimen cut out from the thickness center (all dimensions in mm, thickness: 0.08 mm)¹⁴⁾

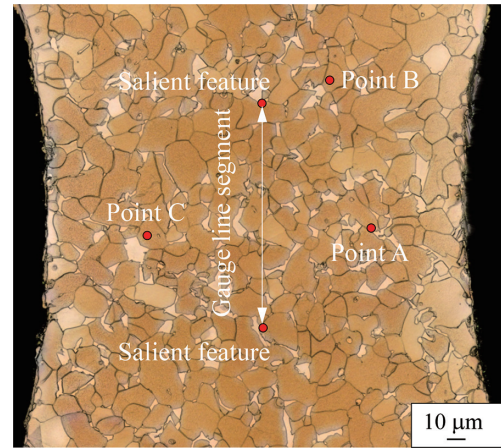


Fig. 10 Micrograph showing the initial microstructure of the *in-situ* specimen that as reference for simulations¹⁴⁾

vided (Fig. 9). In addition, the surface of the specimen was polished and then etched by Le Pera color etchant to distinguish the martensite islands from the ferrite matrix; the martensite was colored white and the ferrite was colored brass yellow. The logarithmic strain in the tensile test was measured based on the distance between two martensite islands separated by 100 μm in the tensile direction (Fig. 10).

3.2 Numerical simulation procedures

A two-level sub-modeling technique was employed for the simulations. At level 1, the entire specimen was modeled subjected to the usual boundary conditions for a tensile test. The nodal displacements at Level 1 were stored at the prescribed time intervals and subsequently used as boundary conditions at the domain of *in-situ* imaging (Level 2). In tensile test analysis to simulate macroscopic deformation behavior, a domain of 1.4 mm in the longitudinal direction from the center of the notch on the specimen was turned into a model and it was divided into 59410 elements (hexahedral solid element) and 72276 nodal points. Displacement of ±0.035 mm was given to both upper and lower ends (Fig. 11). It was supposed that the material was macroscopically homogeneous in this entire analysis. The Swift law that was identified by approximating the tensile test results was used for the steel sheet's work hardening.

$$\sigma_{eq} = K(\epsilon_0 + \epsilon_{eq}^p)^n \quad (4)$$

Where, σ_{eq} is the effective stress, ϵ_{eq}^p is the equivalent plastic strain, K is 1208 MPa, ϵ_0 is 0.003, and n is 0.243. As the solver, V-MulitMat that was static explicit FEM made by RIKEN, Japan was used.^{16, 17)}

Meanwhile, the mesoscale simulation of the domain subject to the *in-situ* observation was only for the center of the observed specimen and an FEM model was created. The image in Fig. 10 was binarized to martensite and ferrite as shown in Fig. 11(a) and the image was divided into 106715 elements (a 5 μm-thick layer of 6-node

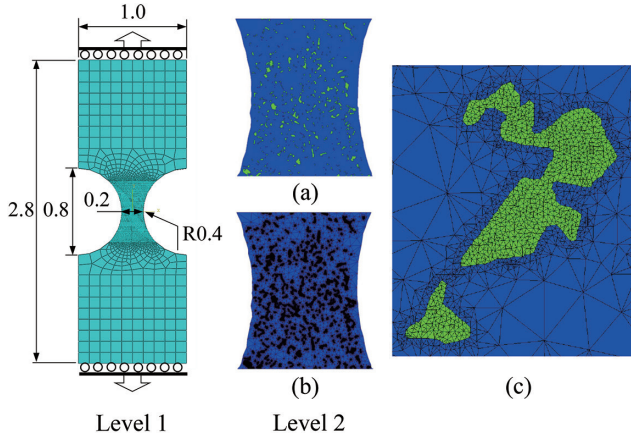


Fig. 11 Left: Front view of 3D-mesh of level1-domain and schematic illustration of the boundary conditions (all dimensions in mm) Right: Generation of mesh of the level2-domain (a) Segmented image, (b) Front of the pentahedric mesh, (c) Showing a higher mesh density around the martensite islands¹⁴⁾

prisms with linear interpolation and selective reduced integration) and 134086 nodal points using VCAD software.^{16,17)} As boundary conditions, the entire analysis' boundary conditions were given to the domain with a thickness of $5 \mu\text{m}$ from the surface (underside of the triangular element) and to the edges, and the degree of freedom on the surface side was not restricted. In addition, it was supposed that each phase was an elasto-plastic material and it was determined that the constitutive law of the material would follow the von Mises yield function and an associated flow rule. In this study, for the work hardening properties of each phase, ferritic single-phase steel and martensite single-phase steel with the same chemical composition as that of each phase composing DP steel were created¹⁵⁾ and approximated by the Swift law and Voce law, respectively.

$$\sigma_{eq} = \sigma_0 + (\sigma_{sat} - \sigma_0) [1 - \exp(-C_Y \varepsilon_{eq}^p)] \quad (5)$$

Where, K is 1208 MPa, ε_0 is 0.003, n is 0.243, σ_0 is 1000 MPa, σ_{sat} is 2650 MPa, and C_Y is 70.

Although many models have been proposed for ductile fracture, the model proposed by Bao-Wierzbicki¹⁸⁾ was used in our study to simulate the fracture of martensite.

$$\varepsilon_{eq}^f = \begin{cases} \frac{C_1}{1+3\eta} & \text{for } -\frac{1}{3} \leq \eta \leq 0 \\ C_2 + (C_2 - C_1)(3\eta - 1) & \text{for } 0 \leq \eta \leq \frac{1}{3} \\ C_2 \exp\left\{-\alpha\left(\eta - \frac{1}{3}\right)\right\} & \text{for } \eta \geq \frac{1}{3} \end{cases} \quad (6)$$

ε_{eq}^f is the equivalent plastic strain at which fracture begins and it is expressed by stress triaxiality ($\eta = \sigma_m / \sigma_{eq}$) for which the average stress (σ_m) is normalized with effective stress (σ_{eq}). Where, C_1 is the equivalent plastic strain that reaches fracture at pure shear ($\eta=0$), C_2 is one that reaches fracture at uniaxial tensile ($\eta=1/3$), and α is the decay parameter.

These material constants were determined as follows by comparing the *in-situ* observation results in the tensile test to the simulation results: $C_1 = C_2 = 0.02$ and $\alpha = 3.0$.¹⁴⁾ In addition, the following formula was used for the damage variable.

$$D(\varepsilon_{eq}^p) = \int_0^{\varepsilon_{eq}^p} d\varepsilon_{eq}^p / \varepsilon_{eq}^f \quad (7)$$

This damage variable (D) can be interpreted as a scale indicating microvoid density and it changes within the range of $0 \leq D \leq 1$. To consider changes in deformation behavior due to the development

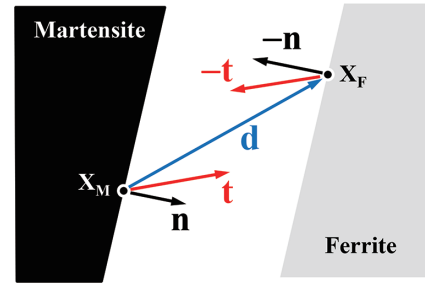


Fig. 12 Modeling the node-to-node contact along the martensite/ferrite interfaces¹⁴⁾ (x_M, x_F : initially coincident points of the martensite/ferrite interface, d : separation vector, t : stress vector)

of microscopic damage, the following V-MultiMat function was used.¹⁶⁾

$$\mathbf{K}_D = (1 - D^2) \mathbf{K} \quad (8)$$

Where, \mathbf{K} is the value of the elemental stiffness matrix at a current Gauss point and \mathbf{K}_D is the weakened value of this matrix.¹⁹⁾

The Decohesion model that Xu-Needleman²⁰⁾ proposed was adopted to express the occurrence and development of fracture at the interface between ferrite and martensite. In this model, double nodal points are arranged at the interface between ferrite and martensite: as the relative displacement (d) that occurs between the nodal points by external force increases, the unifying force (t) changes (Fig. 12). Where, n is the normal direction to the interface, t is the tangential direction, and Φ is a potential expressing the development behavior. The unifying force (t) is expressed with the formula below.

$$t_n = \frac{\partial \Phi}{\partial d_n}, \quad t_t = \frac{\partial \Phi}{\partial d_t} \quad (9)$$

$$\Phi = \Phi_n - \Phi_n (1 + \hat{d}_n) \{1 - q + q \exp(-\hat{d}_t^2)\} \exp(-\hat{d}_n)$$

Where, $\hat{d}_n = d_n / \delta_n$, $\hat{d}_t = d_t / \delta_t$, $\Phi_n = e \sigma_{\max} \delta_n$, $\Phi_t = \sqrt{e} / 2 \tau_{\max} \delta_t$, and $q = \Phi_t / \Phi_n$. There are four material constants: Components at the maximum bond strength (σ_{\max} and τ_{\max}) and relative displacements at that time (δ_n and δ_t). These material constants were determined as follows such that they would reproduce the fracture behavior at the interface between the ferrite and martensite in the *in-situ* observation results: $\sigma_{\max} = \tau_{\max} = 800$ MPa, $\delta_n = 1.0 \mu\text{m}$, and $\delta_t = 0.5 \mu\text{m}$.¹⁴⁾

3.3 Results and considerations

Figure 13 shows the observation and simulation results. The simulation results show that plastic deformation in the martensite tends to be localized at the narrow part of the martensite and the damage variable (D) at this part exceeds 1. A comparison with the *in-situ* observation results shows that the martensite fracture locations almost match and the simulation can predict the locations of voids to be created relatively accurately.

Figure 14(a) shows the *in-situ* observation result when a tensile strain of 28% was applied, showing that black sections were formed on the surface of the specimen. Most of these black sections are near the interfaces between the ferrite and martensite. The black sections are caused by abrupt out-of-plane deformation that occurred on the surface. They can be regarded as damage made on the surface; that is to say, voids formed near the interfaces between the ferrite and martensite. Figure 14(b) shows stress vectors in the tensile direction working on the interfaces between the ferrite and martensite. A comparison with the *in-situ* observation results shows that the locations at which large separation stress occurs in the simulation almost match the fracture locations seen in the *in-situ* observation. However, many factors in the mechanism by which a void is formed near an

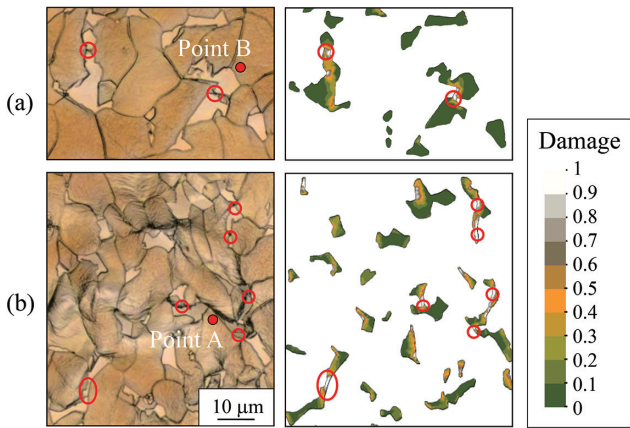


Fig. 13 Comparison of *in-situ* observations and martensite fracture with simulation results¹⁴⁾
(a) At 0.1 gauge strain, and (b) At 0.28 gauge strain
Locations of martensite fracture are highlighted by elliptical red markers

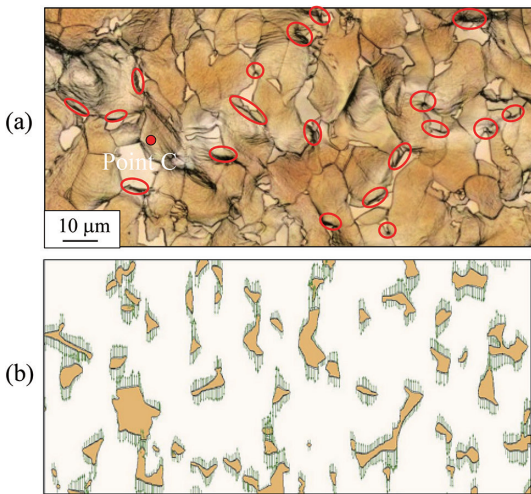


Fig. 14 (a) Micrographs showing the decohesion phenomena recorded at the front surface of the tensile specimen, at 0.28 gauge strain¹⁴⁾
(b) Visualization of the components of the separation vectors along the tensile direction¹⁴⁾

interface have not been clarified, so a more detailed observation is required to verify the simulation results obtained in this study.

4. Simulation of Material Properties of DP Steel in Consideration of Damage

A numerical simulation was carried out to study the effects of strength differences between the soft and hard phases of DP steel on the material properties by finite element analysis based on the continuum damage mechanics (CDM). The user subroutine of general-purpose finite element analysis software ABAQUS™ was used for the analysis.

4.1 Damage evolution equation based on the continuum damage mechanics

CDM is a theoretical system that is based on the continuum mechanics and that has been widely used recently to simulate a wide range of discontinuous behavior, such as fracture and crack propagation.^{21, 22)} The reduction rate of an area that burdens force reduced

due to the formation and growth of microvoids in a material is defined as the damage variable (D). Damage is considered by allowing the damage variable (D) to affect the state variable such as stress and strain. When the damage variable (D) reaches the damage critical value (D_{cr}), which is a material constant, a macroscopic crack occurs and the material breaks. The formula below is Lemaitre's damage evolution equation.²¹⁾

$$dD = \frac{\sigma_{eq}^2}{2SE(1-D)^2} \left(\frac{2}{3}(1+\nu) + 3(1-2\nu) \left(\frac{\sigma_m}{\sigma_{eq}} \right)^2 \right) d\varepsilon_{eq}^p H(\varepsilon_{ac}^p - \varepsilon_{pd}) \quad (10)$$

Where, dD is the damage variable increase, σ_{eq} is the effective stress, E is the Young's modulus, ν is the Poisson's ratio, σ_m is the hydrostatic stress, $d\varepsilon_{eq}^p$ is the equivalent plastic strain increment, ε_{ac}^p is the cumulative equivalent plastic strain, and S and ε_{pd} are the material constants. H is the Heaviside function that indicates when the cumulative equivalent plastic strain (ε_{ac}^p) reaches a certain threshold, a microvoid is formed in the material. In addition, S is a material constant related to the damage evolution rate; As it is smaller, the damage evolution rate is larger. For details of CDM, refer to document 21).

4.2 Analysis model

For the sake of simplification in this study, a mesoscale model was used where the second phase that was spherical islands with different sizes that were separated from each other was randomly arranged in a phase (red in Fig. 15). The volume fraction of the second phase was 20%. The analysis domain is a cube with 100- μm sides and a tensile load was applied. Specifically, displacement in the tensile direction on the bottom was restricted and forced displacement of 30 μm was applied in the tensile direction on the facing top (figure on the left in Fig. 15). To reduce the boundary effect, the Navier hypothesis was applied to the sides and the sections within 10 μm from the top, bottom, and side faces were determined as a domain to reduce the boundary effect and the damage rate was reduced to approximately one fifth there (material constant S was quintupled). In addition, the remaining domain that was obtained by excluding the domain to reduce the boundary effect from the analysis domain was determined as the evaluation domain. Stress was calculated from the sectional force perpendicular to the tensile direction that occurred in the evaluation domain. Strain was calculated from the tension displacement (average of variations of the distance between the top and bottom faces in the evaluation domain) in the evaluation domain. The finite element was a cube with 1- μm sides. It was supposed that the subsequent yield function to which the damage variable (D) was taken into account would follow general Swift law and elastic deformation would follow general Hooke's

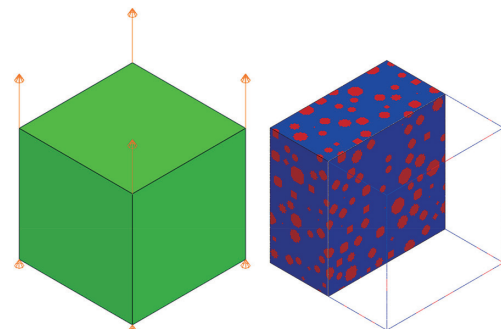


Fig. 15 Analysis model

law.

4.3 Effects of non-metallic inclusions in DP steel on material properties²³⁾

It was assumed that the second phase (spherical islands) in the analysis model in the previous paragraph was a hard phase and the other first phase was a soft phase, and that a nonmetallic inclusion (hereinafter, inclusion) existed in the soft phase. Based on such assumption, how the volume fraction and shape of an inclusion would affect material properties was evaluated. It was assumed that the unifying force at the interface between the inclusion and soft phase was weak and the inclusion was handled as an initial vacancy in the material (material constants were determined such that it would be a vacancy immediately after tensile load). In addition, the hard phase in this model is spherical and thereby will not incur much damage. Therefore, it was assumed for the sake of simplification that microvoids would be formed only in the soft phase (material constants were determined such that the hard phase would not become damaged). If the hard phase is not a simple ball and in a complicated form where hard phases are partially linked, the fracture of the hard phase may need to be taken into account.²⁴⁾

In addition, to reduce the calculation cost of this evaluation, the length of the evaluation domain in the width direction was determined as 30 μm. Various models were used in which the volume fraction of the second phase (hard phase) was constant and the strength difference between the phases varied. **Table 2** lists the material constants of the phases of both materials (A and B) and inclusion. The Young’s modulus (*E*) (206 GPa) and Poisson’s ratio (*ν*) (0.333) were the same. In other words, material A is the case where the strength difference between the phases is small (when the *K* value of the hard phase is 1350 MPa) and material B is the case where the strength difference between the phases is large (when the *K* value of the hard phase is 3600 MPa).

Figures 16 and 17 show the evaluation results of the ultimate tensile strength (UTS), uniform elongation (*E_uts*), and total elongation (*E_f*) under the conditions below: When the volume fraction of the inclusion is 0.02% (*V_I*=0.0002), 0.1% (*V_I*=0.001), and 0.2% (*V_I*=0.002) and in the case where the volume fraction of the inclusion is 0.1% and the shape of the inclusion is changed (the aspect ratio is four times [stretched in a long, narrow way in the direction perpendicular to the tensile direction]) (*V_I*=0.001, X). The evaluation values have been standardized based on the results in the case without inclusions. These results show that the volume fraction and shape of the inclusion have negligible effects on the ultimate tensile strength and uniform elongation within the range of this study.

Meanwhile, regarding the total elongation, the figure shows that when the strength difference between the phases is large, the sensitivity is low; and when the strength difference between the phases is small, the sensitivity is high. It was simulated that the total elongation would significantly deteriorate when the shape was changed.

Table 2 Material constants

	<i>K</i> [MPa]	ϵ_0 [-]	<i>n</i> [-]	ϵ_{pd} [-]	<i>S</i> [MPa]	<i>D_cr</i> [-]
Soft	900	0.005	0.117	0.117	10.0	0.064
Hard	1350	0.004	0.040	10.0	1.0	0.380
	3600					
Non-metallic inclusion	900	0.004	0.140	0.01	1.0	0.010

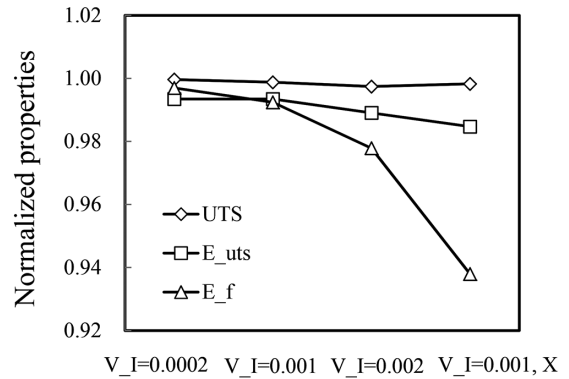


Fig. 16 Effect on material properties of volume fraction and shape of inclusion²³⁾ (in case that strength differential between phases is lower)

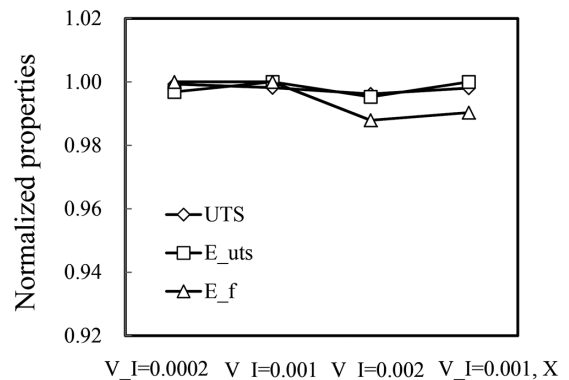


Fig. 17 Effect on material properties of volume fraction and shape of inclusion²³⁾ (in case that strength differential between phases is higher)

This is possibly because when the strength difference between the phases is small, the hard second phase bears deformation, so deformation concentration due to the strength difference between the phases does not occur much and thereby the effects of the deformation concentration and fracture caused by the inclusion appear more: On the other hand, when the strength difference between the phases is large, the hard phase does not deform, so deformation largely concentrates in the entire soft phase and thereby fracture due to the strength difference between the phases occurs more easily, which obscures the effects of the inclusion.

4.4 Effects of strength difference between the phases of DP steel on material properties

Next, how strength difference between the phases would affect material properties was evaluated assuming that the second phase (spherical islands) in 4.2 was a hard phase (the soft phase’s volume fraction was 80%) as is the case with 4.3. In addition, the effects were evaluated in another case where the second phase was assumed as a soft phase (the hard phase’s volume fraction was 80%). In such evaluation, it was assumed that there were no inclusions unlike the case in 4.3. In addition, the occurrence of microvoids in the hard phase was taken into account, because when the main part was the hard phase, the hard phase would possibly become damaged easily because it was not spherical. **Table 3** lists the combinations of each phase of C1 to C3 (materials mainly consisting of the soft phase) and D1 to D3 (materials mainly consisting of the hard phase). **Table 4** lists the material constants of the phases. The Young’s modulus (*E*)

Table 3 Materials and phases

	Phase1/Hardness [HV]	Phase2/Hardness [HV]	ΔHV
C1	Soft 3/310	Hard 1/1000	690
C2	Soft 2/295	Hard 1/1000	705
C3	Soft 1/280	Hard 1/1000	720
D1	Hard 2/720	Soft 6/540	180
D2	Hard 2/720	Soft 5/370	350
D3	Hard 2/720	Soft 4/200	520

Table 4 Material constants

	K [MPa]	ϵ_0 [-]	n [-]	ϵ_{pd} [-]	S [MPa]	D_{cr} [-]
Hard 1	3650	0.004	0.040	0.040	1.0	0.99
Hard 2	2505	0.004	0.050	0.050	5.0	0.99
Soft 1	1200	0.004	0.240	0.240	1.0	0.99
Soft 2	1260	0.004	0.240	0.240	1.0	0.99
Soft 3	1300	0.004	0.240	0.240	1.0	0.99
Soft 4	791	0.004	0.155	0.155	5.0	0.99
Soft 5	1363	0.004	0.088	0.088	5.0	0.99
Soft 6	1934	0.004	0.064	0.064	5.0	0.99

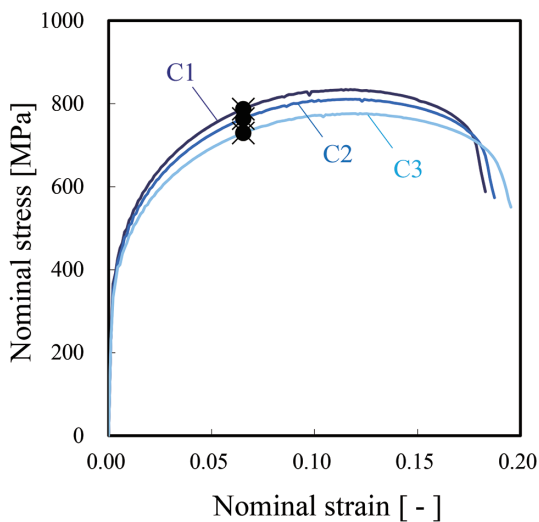


Fig. 18 Effect on stress strain relation of strength differential between phases (in case that volume fraction of soft phase is 80%)

(206 GPa) and Poisson’s ratio (ν) (0.333) were the same.

Figure 18 shows the stress-strain curves of C1 to C3 (materials mainly consisting of the soft phase). Figure 19 shows those of D1 to D3 (materials mainly consisting of the hard phase). The black dots in the figures indicate points of initial fracture of the soft phases (damage variable $[D]$ reached the damage critical value $[D_{cr}]$). The \times signs in the figures indicate such points in the hard phases. When the materials mainly consist of the soft phase, as the soft phase is stronger, that is to say, as the strength difference between the phases is smaller, the materials’ tensile strength is larger, while the uniform elongation and total elongation tend to decrease. This may be because the effect of higher strength of the soft phase was directly reflected to the properties of the DP steel.

On the other hand, when the materials mainly consist of the hard phase, as the soft phase is stronger, that is to say, as the strength difference between the phases is smaller, the materials’ tensile strength

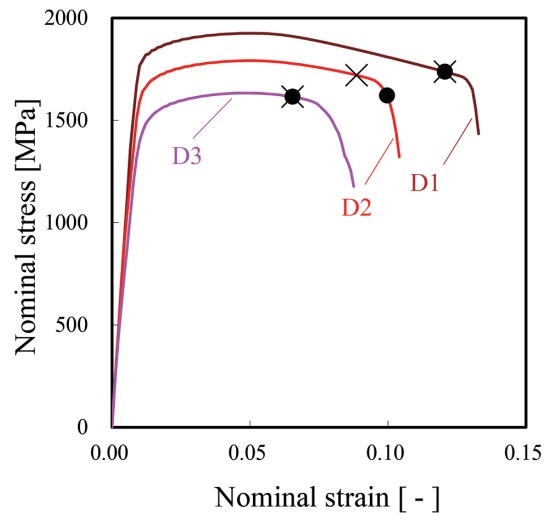


Fig. 19 Effect on stress strain relation of strength differential between phases (in case that volume fraction of soft phase is 20%)

is larger, while the total elongation tends to increase unlike the materials mainly consisting of the soft phase. However, at the analysis level of this study, no changes were seen for the uniform elongation. As described above, the observed effects of the strength difference between the phases on the material properties varied between the materials mainly consisting of the soft phase and those mainly consisting of the hard phase. This may be because when the material mainly consists of the hard phase, the soft phase in smaller volume bears more deformation; thereby when the soft phase (spherical islands) is weaker, they act like spherical vacancies; and as a result, the material strength lowers and deformation concentration in the surrounding hard phase is induced, which decreases the ductility by early fracture of the hard phase.

5. Conclusions

We clarified the characteristics of microscopic structure changes on IF steel in uniaxial and equal biaxial tensile deformation by *in-situ* SEM observation and considered the mechanism of anisotropic work hardening behavior by the crystal plasticity FEM analysis. We also showed that by the mesoscale FEM analysis to which the actual structure of DP steel was reflected, martensite fracture in the structure and fracture at the interfaces between ferrite and martensite can be reproduced and we showed that by continuum damage FEM, DP steel’s ductile fracture varies by the relativization of the hardness of the hard phase and soft phase.

Thus, mesoscale finite element analysis can consider the material structure’s heterogeneous structure and can evaluate the elementary processes of deformation, clarification of its mechanism, materials’ microscopic structure changes, and macroscopic deformation characteristics. Seamless simulation technologies for simulating materials’ structure, deformation characteristics, and the performance of final products need to be developed in the future by combining cutting-edge experimental analysis technologies with computational science. Such multiscale simulation technologies would make it possible to design optimum structure to realize the required final performance and material properties and to consider manufacturing processes to achieve such. We will work to develop such simulation technologies, materials that can satisfy increasingly sophisticated needs, and technologies to use such materials in the future.

References

- 1) Ushioda, K.: J. Jpn. Soc. Technol. Plast. 58, 357–360 (2017)
- 2) Kuwabara, T. et al.: J. Mater. Process. Technol. 80, 517–523 (1998)
- 3) Kuwabara, T.: Int. J. Plast. 23, 385–419 (2007)
- 4) Kuwabara, T. et al.: Acta Mater. 50, 3717–3729 (2002)
- 5) Ikeda, S. et al.: Tetsu-to-Hagané. 90, 1016–1022 (2004)
- 6) Kubo, M. et al.: ISIJ Int. 56, 2259–2266 (2016)
- 7) Ikematsu, Y. et al.: CAMP-ISIJ. 18, 553 (2005)
- 8) Kubo, M. et al.: ISIJ Int. 56, 669–677 (2016)
- 9) Hoc, T. et al.: Int. J. Plast. 17, 65–85 (2001)
- 10) Tsunemi, Y. et al.: Procedia Engineering. 207, 2095–2100 (2017)
- 11) Taylor, G.I.: J. Inst. Met. 62, 307–324 (1938)
- 12) Jiang, J. et al.: Int. J. Plast. 69, 102–117 (2015)
- 13) Uenishi, A. et al.: Shinnittetsu Giho. (392), 58–63 (2012)
- 14) Matsuno, T. et al.: Int. J. Plasticity. 74, 17–34 (2015)
- 15) Matsuno, T. et al.: ISIJ Int. 54, 938–944 (2014)
- 16) Alves, J. L. et al.: Proc. Symp. on the VCADSystem. Res. Program 2009. Phys. Chem. Research (RIKEN), p. 64–65
- 17) Alves, J.L. et al.: Proc. Symp. on the VCADSystem. Res. Program 2010. Phys. Chem. Research (RIKEN), p. 165–168
- 18) Bao, Y. et al.: Int. J. Mech. Sci. 46, 81–98 (2004)
- 19) Xue, L. et al.: Int. J. Solids Struct. 44, 5163–5181 (2007)
- 20) Xu, X. P. et al.: Modell. Simul. Mater. Sci. 1, 111–132 (1993)
- 21) Lemaitre, J.: A Course on Damage Mechanics. Springer-Verlag, 1992
- 22) Murakami, S. et al.: Trans. Jpn. Soc. Mech. Eng. 60-578, A, 2398–2403 (1994)
- 23) Suwa, Y. et al.: Materials Science Forum. 706–709, 1527–1532 (2012)
- 24) Toda, H. et al.: Acta Mater. 126, 401–412 (2017)



Shigeru YONEMURA
Senior Researcher, Dr. Eng.
Application Technology Research Lab.
Steel Research Laboratories
20-1 Shintomi, Futtsu City, Chiba Pref. 293-8511



Akihiro UENISHI
General Manager, Head of Lab., Dr.
Sheet & Coil Research Lab.
Steel Research Laboratories



Masahiro KUBO
Researcher
Nagoya R & D Lab.



Satoshi HIROSE
Senior Researcher, Ph.D.
Application Technology Research Lab.
Steel Research Laboratories



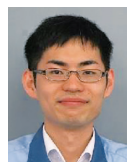
Yusuke TSUNEMI
Researcher
Application Technology Research Lab.
Steel Research Laboratories



Yoshihiro SUWA
Senior Researcher, Dr. Eng.
Fundamental Metallurgy Research Lab.
Advanced Technology Research Laboratories



Daisuke MAEDA
Senior Researcher
Sheet & Coil Research Lab.
Steel Research Laboratories



Takashi YASUTOMI
Application Technology Research Lab.
Steel Research Laboratories